# Polyvalent Machine-Learned Potential for Cobalt: from Bulk to Nanoparticles

Marthe Bideault
*Materials Design SARL, 42 avenue Verdier, 92120 Montrouge, France*

Jérôme Creuze
*ICMMO/SP2M, Université Paris-Saclay, UMR 8182, 17 avenue des Sciences, 91400 Orsay, France*

Ryoji Asahi
*Institute of Materials Innovation, Nagoya University, Nagoya 464-8603, Japan*

Erich Wimmer
*Materials Design SARL, 42 avenue Verdier, 92120 Montrouge, France*
(Dated: April 4, 2024)

We present the development of a quadratic Spectral Neighbor Analysis Potential (q-SNAP) for ferromagnetic cobalt and its applications to bulk phases, surfaces, and nanoparticles. Trained on Density Functional Theory calculations using the Perdew-Burke-Ernzerhof (DFT-PBE) functional, this machine-learned potential enables simulations of large systems over extended time scales across a wide range of temperatures and pressures at near DFT accuracy. It is validated by closely reproducing the phonon dispersions of hexagonal close-packed (hcp) and face-centered cubic (fcc) Co, surface energies, and the relative stability of nanoparticles of various shapes. Thermal expansion and the melting point of Co computed with this potential are close to experimental values. Furthermore, this machine-learned potential goes beyond the capabilities of simpler N-body potentials by capturing nuanced properties such as vacancy formation energies on nanoparticle vertices. This accuracy and versatility make the potential suitable for a wide range of applications, including catalysis.



## I. INTRODUCTION

Elemental cobalt is a ferromagnetic transition metal that exists in two allotropic forms: at ambient conditions, the most stable phase is $\alpha$-Co, which crystallizes in a hexagonal close-packed structure. At higher temperatures, face-centered cubic $\beta$-Co becomes the most stable form. Matter *et. al.* give a transition temperature of 693 K [1]. Cobalt metal is a relatively hard material with a melting point of 1768±1 K [2].

Cobalt is used in a wide range of applications including wear-resistant high-strength alloys [3], Li-ion batteries [4], magnetic recording [5], permanent magnets [6], medical implants [7], dentistry [8], and radiotherapy [9]. In catalysis, Co is typically employed in the form of nanoparticles [10].

In fact, nanoparticles have revolutionized the field of catalysis with their unique size-dependent properties and high surface-to-volume ratio [11]. These nanoscale materials offer unprecedented opportunities for accelerating reactions, enhancing selectivity, and enabling greener and more efficient processes, while minimizing the amount of catalytic material.

In support of further development and optimization of catalysts, accurate atomic-scale simulations are highly valuable. Density Functional Theory (DFT) [12] is a preferred approach for systems featuring complex chemistry in a great variety of structural environments. However, these calculations are computationally demanding, limiting time scale and model size to few hundreds of picoseconds and atoms, respectively. Often, temperature effects are omitted by focusing on structures with minimum total energy. While a wealth of valuable information has been gained from this type of static ground state approaches, more realistic models are needed to include dynamic effects, especially in catalytic processes involving nanoparticles.

Interatomic potentials such as those obtained with the embedded atom method (EAM) [13] enable simulations of systems containing hundreds of thousands of atoms over time frames up to microseconds, but they are not suited for complex chemistries and substantial variations in the atomic environment. The rise of machine-learned potentials (MLPs) has opened exciting novel avenues [14–16]. Training these MLPs on data from *ab initio* calculations yields force fields usable at the same scales as empirical potentials, while maintaining the generality and accuracy of DFT.

Each of these new interatomic potentials is founded on a descriptor of atomic environments and a model that links them to local energies. Descriptors are mathematical entities invariant under translation, rotation, and permutation of atoms of the same type. A diverse array of descriptors exists, such as the bispectrum (BSO(4)) [17], the Smooth Overlap of Atomic Positions (SOAP) [18], and the Atomic Cluster Expansion (ACE) [19]. Likewise, models span from simple linear regression to multilayer neural networks [17, 19–22]. Thompson *et al.* [20] demonstrated a linear relationship between bispectrum descriptors and system observables (energy, forces and stress), leading to the introduction of the Spectral Neighbor Analysis Potential (SNAP). Later, they showed that adding quadratic terms to the model (leading to a q-SNAP) offers improved accuracy [23].

In this article, we present the construction of a q-SNAP for cobalt, dedicated to bulk, surface, and nanoparticle modeling. To demonstrate its quality, we show that it reproduces phonon dispersions and surface energies of hexagonal close-packed (hcp) and face-centered cubic (fcc) Co, as well as the relative stability of nanoparticles of various shapes at the accuracy of DFT. Dynamical properties including the $\alpha$-$\beta$ phase transition, thermal expansion, and the melting point are predicted in remarkable agreement with experimental values. Additionally, we compare the capabilities of this q-SNAP with those of one of the most widely used EAM potential for Co [24] in predicting quantities that can be critical in catalysis, such as surface energies and the vacancy formation energies on nanoparticle vertices.

The paper is organized as follows: in Section II, we outline the methods employed, beginning with a brief recapitulation of the q-SNAP formalism, followed by the approach used for fitting and testing the potential. In Section III, we demonstrate the capabilities of the new q-SNAP in terms of nanoparticle modeling. We start by analyzing the relative stability of nanoparticles of different shapes as a function of their size. Next, we compare the predictive performance of the q-SNAP and EAM potentials in determining surface energies and vacancy formation on vertices. Subsequently, we showcase the predictive capability of q-SNAP by computing the cobalt melting point through the melting of nanoparticles of increasing size, emphasizing its suitability for dynamic processes. Finally, we present our conclusions in Section IV.

## II. CONSTRUCTION OF THE POTENTIAL

### A. SNAP formalism

An interatomic potential connects local descriptors of the atomic environment of each atom to observables such as the total energy of the entire system, forces on each atom, and stress tensors. In the case of SNAP, bispectrum descriptors are used to represent the atomic environments. In this approach, the density of neighbor atoms around a central atom $i$ at location $\mathbf{r} < R_{cut}$ is a sum of Dirac functions, $\delta$, located in a three-dimensional space:

$$\rho_i(\mathbf{r}) = \delta(\mathbf{r}) + \sum_{r_{ii'}<R_{cut}} f_c(r_{ii'}) w_{i'} \delta(\mathbf{r} - \mathbf{r}_{ii'}) \qquad (1)$$

where $\mathbf{r}_{ii'}$ is the vector joining the two neighboring atoms $i$ and $i'$, $w_{i'}$ is a dimensionless coefficient used to differentiate between atoms of different types (in our case, it is always set to one since the q-SNAP is for pure cobalt) and the function $f_c(r)$ ensures that the contribution of each neighbor atom smoothly tends to zero at a cutoff radius $R_{cut}$.

The density is then expanded in spherical harmonics used as basis functions:

$$\rho_i(r) = \sum_{j=0}^{\infty} \sum_{m,m'=-j}^{j} u^j_{m,m'} U^j_{m,m'}(\theta, \phi, \theta_0), \qquad (2)$$

where $\theta_0$ is a third polar angle used to map the radial distance $r$ as

$$\theta_0 = \theta_0^{max} \frac{r}{R_{cut}}. \qquad (3)$$

The coefficients $u^j_{m,m'}$ are given by the inner product of the neighbor density with the basis functions. However, these coefficients are not invariant under rotation, rendering this simple expansion in spherical harmonics not directly applicable. This issue is resolved by introducing a bispectrum of spherical harmonics, which is rotationally invariant:

$$B_{j_1,j_2,j} = \sum_{m_1,m_1'=-j_1}^{j_1} \sum_{m_2,m_2'=-j_2}^{j_2} \sum_{m,m'=-j}^{j} \left(u^j_{m,m'}\right) \qquad (4)$$

$$C^{jm}_{j_1 m_1 j_2 m_2} \times u^{jm'}_{j_1 m_1', j_2 m_2'} u^{j_1}_{m_1', m_1} u^{j_2}_{m_2', m_2}, \qquad (5)$$

where $C$ are Clebsch-Gordan coefficients. These bispectrum descriptors are finally invariant under translations, rotations and permutations. $J_{max}$ is a crucial parameter that determines the number of distinct bispectrum descriptors with indices $j_1, j_2, j < J_{max}$. Increasing its value enhances the detailed description of the chemical environment, at the expense of computational cost. Moreover, it should be noted that excessively increasing $J_{max}$ could lead to overfitting, a topic further discussed in section II B 2.

Once all bispectrum coefficients are determined, they are employed to compute the system's observables. The q-SNAP energy of an atom $i$ is expressed as

$$E^i_{\text{q-SNAP}}(\mathbf{r}^N) = \beta \cdot \mathbf{B}^i + \frac{1}{2}\left(\mathbf{B}^i\right)^T \cdot \alpha \cdot \mathbf{B}^i, \qquad (6)$$

where $\mathbf{B}^i$ are bispectrum descriptors of atom $i$ and $\alpha$ and $\beta$ two sets of coefficients that are optimized during the fitting process using a regression. Linear SNAP only deals with the linear part, focusing solely on optimizing the $\beta$ coefficients. The dimension of the vectors $\mathbf{B}^i$ is related to $J_{max}$. Forces and stresses are expressed as first and second derivatives of the energy in equation 6 with respect to positions, respectively. Further details about the q-SNAP formalism can be found in Refs. 20 and 23.

### B. Fitting process

#### 1. *Training set*

The training set is initially created by performing *ab initio* calculations on a set of structures that represent

cobalt in all relevant configurations. Four crystallographic phases are considered: hcp, fcc, bcc and $\omega$. Unit cells of these phases are deformed in all directions up to 1% strain. Supercells and surfaces are also constructed. Various defects, such as interstitials and vacancies, are introduced into selected supercells, while adatoms, vacancies, and steps are incorporated into certain surface structures. Additionally, we generated icosahedra, truncated octahedra, cuboctahedra, decahedra, hcp, and spherical nanoparticles, each containing up to a few hundred atoms, with defects such as vacancies and adatoms also included. Subsequently, all structures are subjected to molecular dynamics simulations at temperatures up to 1200 K. Furthermore, also liquid structures are included. The EAM potential developed by Pun *et. al.* [24] is used to generate long trajectories with highly uncorrelated configurations. It has been found [21] that the inclusion of highly out-of-equilibrium configurations increases the robustness of the potential.

Additionally, we noticed that including small nanoclusters ranging from 2 to 30 atoms improves the potential's robustness. Indeed, these clusters possess bispectrum descriptors that significantly differ from those of any bulk phase. In surface studies, this type of information is crucial since molecular dynamics simulations at high temperatures can easily lead to the presence of highly undercoordinated atoms, such as adatoms. A training set without these nanoclusters results in a q-SNAP that is unable to model such systems, due to an extreme increase in energy for some atoms of these special configurations.

Furthermore, we included a larger number of icosahedra compared to truncated octahedra and hcp nanoparticles, given their non-crystalline structure without any equivalent in the bulk. Otherwise, they would have been underrepresented in the training set, whereas it is often the most stable morphology for transition metal nanoparticles of a few dozen to a few hundreds atoms [25]. We chose not to increase the representation of decahedra because they are inherently unstable for cobalt [26] and fall outside the scope of our study.

The bispectrum descriptors are computed for all these configurations and are labeled by energy, forces, and stress obtained from *ab initio* calculations. Spin-polarized single point energy calculations are performed using the Vienna Ab Initio Simulation Package (VASP) [27, 28] with the Perdew-Burke-Ernzerhof (PBE) exchange-correlation functional [29] based on a generalized gradient approximation (GGA) [30], as integrated in the *MedeA* materials modeling environment [31]. The core electrons up to the $3p$ level were frozen and their interactions with the remaining nine valence electrons were described using the projector augmented wave method (PAW) [32]. A plane-wave energy cutoff of 300 eV was used and the k-spacing in the Brillouin zone was set to 0.2 $Å^{-1}$ in the periodic directions, while only one k-point was used for non-periodic directions. The Methfessel-Paxton scheme [33] with a smearing width of 0.2 eV was employed for the integration over the Brillouin zone. To reduce the noise in the forces, an additional support grid was used for the evaluation of the augmentation charges. The SCF convergence criterion was set to $10^{-5}$ eV. To avoid interactions due to the periodic boundary conditions, a vacuum space of 15 Å was set in the non-periodic directions of the cell. The ratios of energy *vs.* forces and stresses in the training set are shown in Table. I for each structure type.

TABLE I. Details of the different classes used in the training set. The first column describes the class, the second one gives the number of atoms in the cells used for DFT-PBE calculations, and the three last columns correspond to the total number of energies $n_E$, forces $n_F$, and stresses $n_S$ used for the training/validation procedure.

| Content | Atoms | $n_E$ | $n_F$ | $n_S$ |
|---|---|---|---|---|
| Unit cells | 2-6 | 204/22 | 2640/252 | 1224/132 |
| MD bulk | 32-60 | 227/25 | 34110/3762 | 1362/150 |
| Defaults | 55-127 | 22/2 | 6300/450 | 132/12 |
| Surfaces | 10-288 | 99/11 | 37866/3846 | 594/66 |
| Nanoparticles | 2-308 | 394/43 | 127278/13134 | 2364/258 |

#### 2. *Optimization of fitting parameters*

Using the Machine-Learned Potential Generator (MLPG) of the *MedeA* materials modeling environment [31], the q-SNAP model [20, 23] was trained on the data from DFT-PBE calculations using the least squares method. To achieve the best fit, also the band limit ($2 \times J_{max}$) and the radial cutoff needed to be optimized. To this end, a test set containing 10% of the training configurations was extracted from the training set, and multiple q-SNAPs with different complexities were created. For each q-SNAP, the root mean square error (RMSE) between the training and test sets was computed. The higher the complexity of the descriptors, the more the RMSE on the training set will be reduced. However, there comes a point where the error on the test set starts to increase again [34]. The optimal complexity is thus the one that minimizes the RMSE on the test set. For cobalt with our datasets, a band limit of 8 ($J_{max} = 4$) and a radial cutoff of 5.0 Å are the optimal values. During the fit, weights on forces and stresses were 0.01 and $10^{-6}$ respectively. Fig. 1 shows the training and validation errors on energy and forces of the final fit. The errors are detailed in Table II.

### C. Validation on bulk and surface properties

We assessed the capability of the q-SNAP to accurately reproduce results obtained from periodic DFT-PBE calculations. To achieve this, numerous properties were computed and analyzed. The computational methodologies employed to calculate these properties are detailed

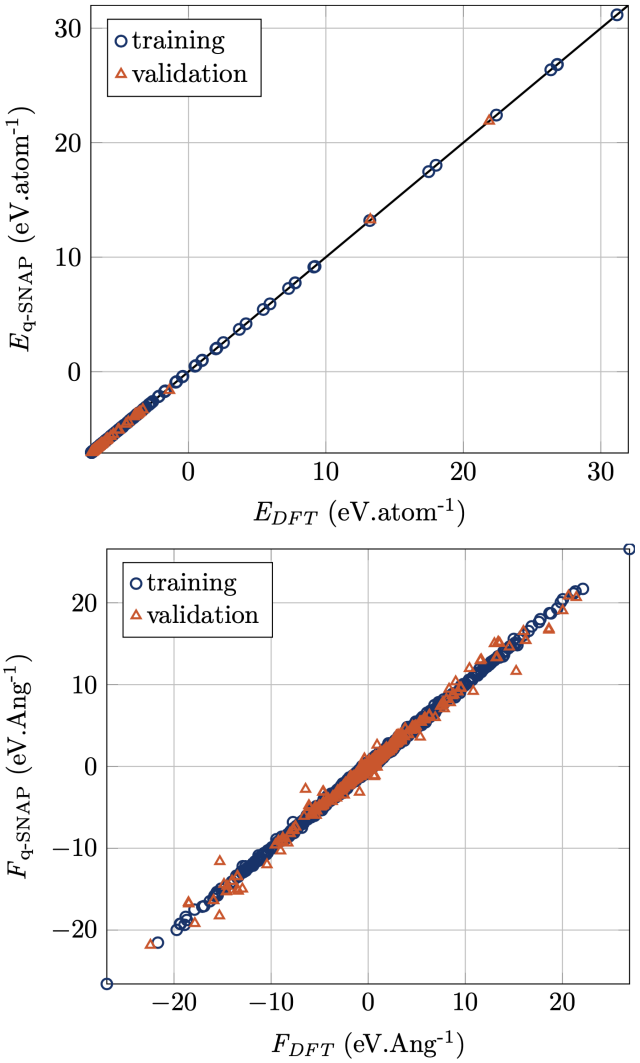


FIG. 1. (Color online) q-SNAP predictions on the training observables compared with DFT-PBE for energies and forces.

below. DFT-PBE calculations were carried out using the parameters outlined in section II B. For structure optimizations, we used the conjugate gradient algorithm with a convergence criterion of 0.02 eV.Å$^{-1}$. The LAMMPS molecular dynamics package [52] was employed to obtain the results based on the q-SNAP. Structure minimizations were also performed using the conjugate gradient

TABLE II. Training and validation errors.

| Type | Group | Unit | MAE | RMSE | $R^2$ |
|---|---|---|---|---|---|
| Energy | train | meV.atom$^{-1}$ | 2.3 | 4.3 | 1.0000 |
| Energy | test | meV.atom$^{-1}$ | 8.1 | 28.6 | 0.9999 |
| Forces | train | meV.Å$^{-1}$ | 30.9 | 54.2 | 0.9957 |
| Forces | test | meV.Å$^{-1}$ | 33.2 | 92.7 | 0.9933 |
| Stress | train | bar | 630 | 1434 | 1.0000 |
| Stress | test | bar | 5931 | 41992 | 0.9998 |

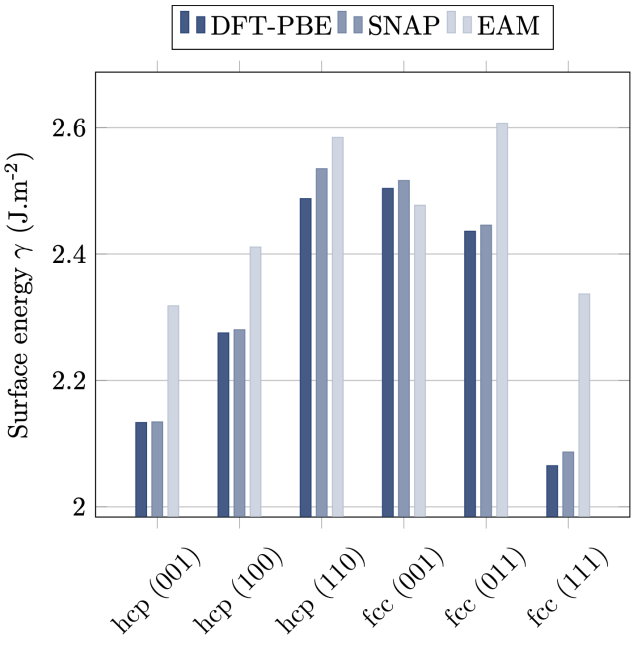


FIG. 2. (Color online) Surface energies calculated with the q-SNAP and compared with those obtained by DFT-PBE and EAM potential [24] values.

algorithm, with a convergence criterion of $10^{-3}$ eV.Å$^{-1}$. During the molecular dynamics simulations, a time step of 2 fs was employed, and the Nosé-Hoover thermostat and barostat were used with dampings of 200 and 2000 fs to control temperature and pressure, respectively.

Tables III and IV compare the experimental values of hcp and fcc cobalt with those obtained with q-SNAP, DFT-PBE and EAM [24]. The q-SNAP results shown in these tables reflect the accuracy of the DFT-PBE level of theory for calculations at $T = 0$ K. The EAM potential was fitted to reproduce experimental data, typically measured at ambient temperature. This explains the better agreement of the EAM results for structural and elastic properties with experimental data compared with the pure DFT-PBE results. However, fitting to specific experimental data runs the risk of introducing uncontrolled errors when using such a potential to compute other properties such as the temperature of phase transitions or surface energies.

The surface energy of phase $\phi$ with Miller indices $(h, k, l)$ is expressed as

$$\gamma_\phi(hkl) = \frac{E_{slab} - E_{bulk_\phi} \times n_{slab}}{2A} \tag{7}$$

were $E_{slab}$ corresponds to the total energy of the slab of area of $A$ containing $n_{slab}$ atoms, and $E_{bulk_\phi}$ to the energy per atom of the minimized bulk cell of phase $\phi$. Slabs were constructed with a vacuum spacing of 15 Å and a minimum thickness of 16 Å. As illustrated in Fig. 2, q-SNAP predicts surface energies for low index orientations that are extremely close to the DFT-PBE values,

TABLE III. Bulk properties of hcp Co.

| Property | Experiment | DFT-PBE | q-SNAP | EAM[a] |
|---|---|---|---|---|
| $a$ (Å) | 2.507[b] | 2.4902 | 2.4899 | 2.5187 |
| $c/a$ | 1.623[b] | 1.6160 | 1.6149 | 1.6103 |
| $C_{11}$ (GPa) | 293[c], 319.50[d], 307.1[e] | 386 | 366 | 311.9 |
| $C_{12}$ (GPa) | 143[c], 166.09[d], 165.0[e] | 151 | 174 | 146.9 |
| $C_{13}$ (GPa) | 90[c], 102.09[d], 102.7[e] | 114 | 118 | 119.6 |
| $C_{33}$ (GPa) | 339[c], 373.60[d], 358.1[e] | 403 | 425 | 359.4 |
| $C_{44}$ (GPa) | 78[c], 82.41[d], 75.5[e] | 97 | 74 | 91.7 |
| $E_v^f$ (eV) | 1.4[f], 1.38[g] | | 1.8222 | 1.49 |
| $T_{hcp-fcc}$ (K) | 690[h], 695[i], 700[j] | | 757 | 717[a] |

[a] Ref. 24
[b] Ref. 35
[c] Ref. 36
[d] Ref. 37
[e] Ref. 38
[f] Ref. 39
[g] Ref. 40
[h] Ref. 41
[i] Ref. 42
[j] Ref. 43

TABLE IV. Bulk properties of fcc Co.

| Property | Experiment | DFT-PBE | q-SNAP | EAM[a] |
|---|---|---|---|---|
| $a$ (Å) | 3.5447[b], 3.568[c] | 3.5103 | 3.5116 | 3.5642 |
| $C_{11}$ (GPa) | 260[d], 225[e], 223[f] | 302 | 328 | 275.7 |
| $C_{12}$ (GPa) | 160[d], 160[e], 186[f] | 173 | 201 | 158.9 |
| $C_{44}$ (GPa) | 110[d], 92[e], 110[f] | 149 | 138 | 108.2 |
| $E_v^f$ (eV) | 1.34 - 1.91[g] | 2.34[h], 1.71[h] | 1.7542 | 1.56 |
| $T_m$ (K) | 1768[i], 1770[j] | | 1695 +/- 15 | 1898[a] |

[a] Ref. 24
[b] Ref. 44
[c] Ref. 45
[d] Ref. 46
[e] Ref. 47
[f] Ref. 48
[g] Ref. 49
[h] Ref. 50
[i] Ref. 51
[j] Refs. 42 and 43

with a maximum difference of 47 mJ.m$^{-2}$ for $\gamma_{hcp}(110)$, whereas the EAM potential leads to much larger deviations, up to 272 mJ.m$^{-2}$ for the $\gamma_{fcc}(111)$. Moreover, the EAM potential finds that the hcp (001) surface is the most stable instead of the fcc (111), and predicts that $\gamma_{fcc}(011) < \gamma_{fcc}(001) < \gamma_{hcp}(110)$. The disparity observed between the EAM potential and the q-SNAP (and DFT-PBE) likely arises from the decisions made during the calibration of the EAM potential, primarily aimed at accurately reproducing bulk properties, as mentioned earlier. It should be mentioned, however, that the PBE level of theory tends to underestimate surface energies of transition metals [53].

A further test of the present q-SNAP is the computation of the thermal expansion of hcp and fcc phases using molecular dynamics simulations in the NPT ensemble at atmospheric pressure between $T$ = 298 and 1200 K. 5x5x5 and 4x4x4 supercells were employed for the hcp and fcc phases respectively. The temperature was incremented linearly in steps of 100 K with an equilibration of 50 ps for each temperature. Only the cell angles were fixed. As illustrated in Fig. 3, the q-SNAP results are in very good agreement with the experimental data from Ref. 41, showing that this interatomic potential reproduces well this property. The small underestimation of the thermal expansion at elevated temperatures may be in part due to the presence of vacancies in the experimental samples while the simulations are preformed for vacancy-free systems.

Phonon dispersions were computed using the phonon module as available in *MedeA* [31], which uses the method described in Ref. 54. The dispersions predicted by the

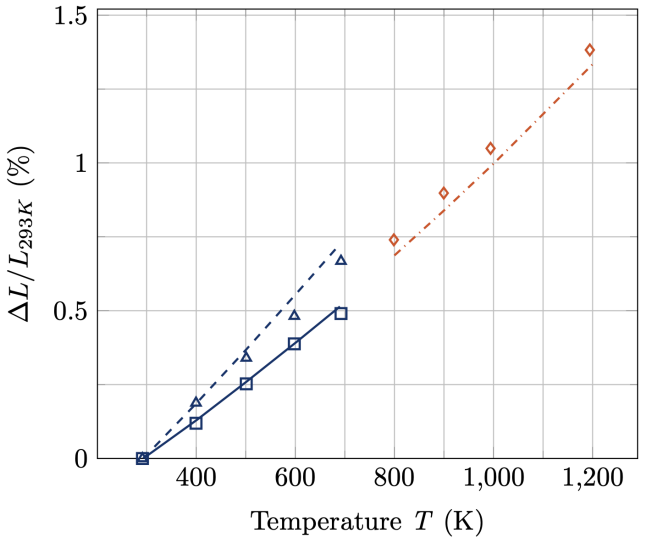


FIG. 3. (Color online) Thermal expansion of hcp and fcc cobalt measured experimentally (lines) and calculated with the q-SNAP (marks). The blue solid line and squares represent the $a$ lattice parameter of hcp cobalt, whereas the dashed line and triangles refer to $c$. The red dash-dotted line and diamonds represent the lattice parameter of fcc cobalt.

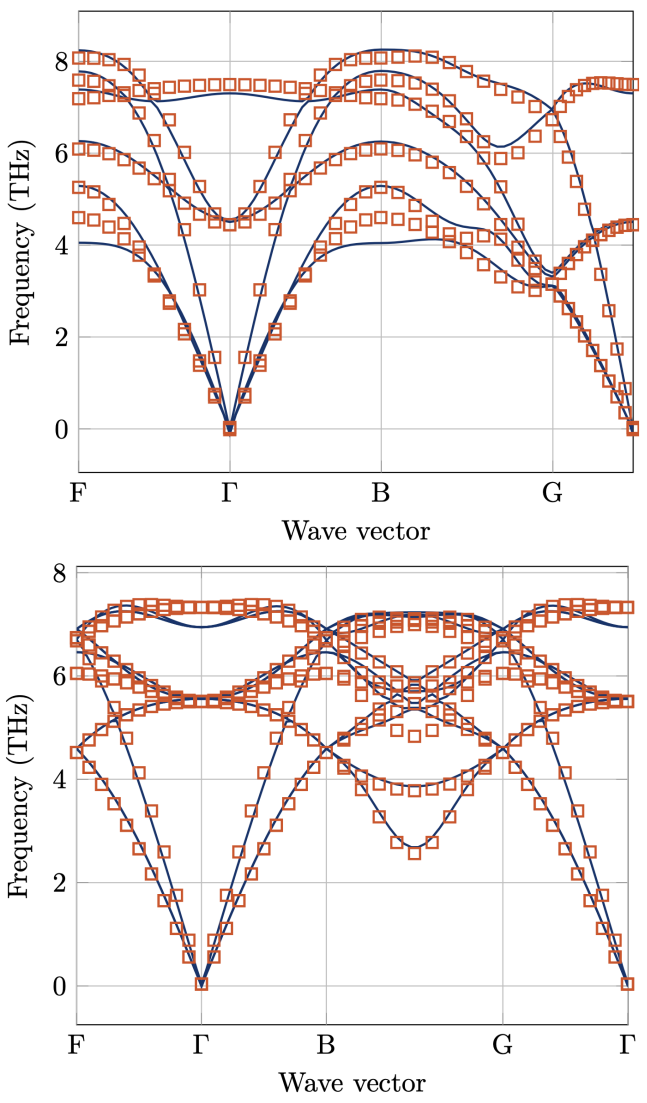


FIG. 4. (Color online) Phonon dispersion curves of hcp (top) and fcc (bottom) cobalt, computed using DFT-PBE (solid lines) and the q-SNAP (squares). Note that these results are obtained in the P1 space group.

q-SNAP are in very good agreement with those predicted by DFT-PBE, as illustrated in Fig. 4 with the highest frequencies being around 8 THz for the hcp phase, consistent with experimental data [55] while the EAM of Pun *et. al.* [24] predicts the highest frequencies to be nearly 11 THz.

An essential benchmark for assessing the efficiency of the potential lies in the computation of the $\alpha$-$\beta$ phase transition. Assuming that the entropic terms are solely vibrational, the Helmholtz free energy $F(T)$ of a given phase $\phi$ is defined as:

$$F_\phi(T) = U(T) + E_{vib,QC}(T) + ZPE - S_{vib}(T)T \quad (8)$$

where $T$ is the temperature, $U$ the total energy of the system, $E_{vib,QC}$ the quantum contribution of the vibrational potential energy, $ZPE$ the zero point energy and $S_{vib}$ the vibrational entropy. The computations of the three last terms rely on the vibrational density of states $DOS(\nu)$, determined via the Fourier transform of the integrated velocity auto-correlation function [56, 57]. Supercells of 1000 and 1008 atoms for the hcp and fcc phases respectively are equilibrated at a given temperature for 170 ps within the NPT ensemble. Subsequently, the velocity auto-correlation function is calculated during two simulations of 25 ps in the NVE ensemble. The Helmholtz free energy of both phases is computed using equation 8, followed by polynomial fitting of the resultant curves to determine $\Delta F_{fcc-hcp}(T)$. As shown in Fig. 5, this function intersects zero at $T = 757$ K, demonstrating rather good agreement with the experimental data, considering that a shift of only 1.6 meV.atom$^{-1}$ would yield a transition temperature close to the experimental value of 693 K [1]. Furthermore, there might be uncertainties also in the experimental value.

The biphased cell method was used to estimate the melting temperature of fcc Co. In the NPT ensemble, following the procedure in [58], a 5x5x20 supercell was equilibrated for 100 ps at 800 K, using NPT molecular dynamics, with only the angles fixed. Subsequently, all atoms with a fractional coordinate $z$ greater than 0.5 were fixed. A 50 ps NPT molecular dynamics simulation was performed at 3000 K to rapidly transform half of the system into a liquid state. During this simulation, only the $z$-direction of the cell was allowed to relax. Then, while still keeping only the $z$-direction free, a third NPT molecular dynamics simulation was conducted at the experimental melting point of 1768 K [2]. This simulation

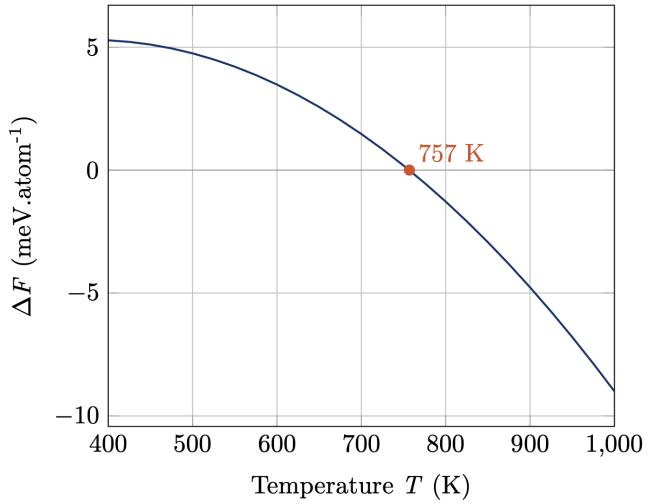


FIG. 5. (Color online) Difference in Helmholtz free energy between the fcc and hcp phases of cobalt as a function of temperature. The predicted phase transition temperature at atmospheric pressure is $T = 757$ K (red dot).

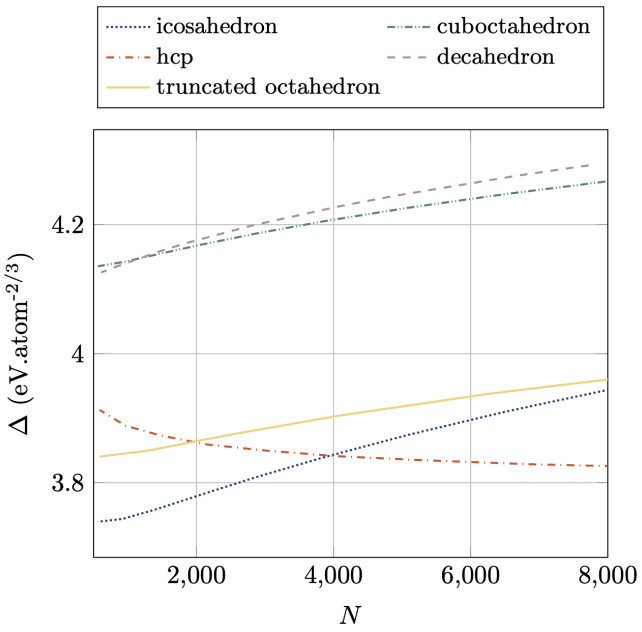


FIG. 6. (Color online) Stability of nanoparticles of different shapes as a function of their size at 0 K.

lasted only 1 ps, which was sufficient to equilibrate the density at the presumed melting temperature without recrystallization. Once this biphased cell was constructed, NPT molecular dynamics simulations of 200 ps were performed at various temperatures. All directions were allowed to relax but the angles were fixed. The melting temperature was determined based on the final state of the final structure. All simulations were conducted at atmospheric pressure. The q-SNAP predicts a melting temperature of 1695 +/- 15 K, which is only 73 K below the experimental value.

In summary of this validation, the present q-SNAP exhibits excellent accuracy in reproducing a broad range of static and dynamic properties of both bulk and surfaces of hcp and fcc cobalt, thus highlighting its robustness and reliability. The agreement with experimental data such as the melting point demonstrates that the underlying level of *ab initio* theory, namely DFT-PBE, provides a remarkably good description of the interatomic interactions in this system.

## III. APPLICATION TO NANOPARTICLES

In the following analysis, our objective was to assert the accuracy and robustness of the present q-SNAP in describing the structure and energetics of nanoparticles. This capability holds substantial importance, particularly in the context of catalysis, where accurate predictions are crucial for understanding and optimizing catalytic processes.

Atoms involved in chemical reactions exist in states far from their equilibrium, adopting configurations of high energy. In heterogeneous catalysis, these reactions take place on surfaces or nanoparticles, where the reactants adsorb on specific sites, which can be an adatom or any other surface pattern with reactive surface atoms [59]. In fact, surface atoms, especially on nanoparticles, dynamically participate in catalytic reactions [60].

As a result, it is crucial to accurately characterize these surfaces and adsorption sites to predict the catalyst's surface state as a function of temperature.

In this part, we will show the capabilities of the present q-SNAP in modeling cobalt nanoparticles, both statically through the relative stabilities of different nanoparticle shapes and the vacancy formation on vertices, and dynamically by examining the melting process.

### A. Morphological stability at $T$=0 K

In terms of the relative stabilities among different shapes, the present q-SNAP predicts the icosahedron to be the most stable shape up to 4000 atoms, after which the hexagonal close-packed (hcp) shape becomes the most stable. This is consistent with experimental observations of icosahedra for small nanoparticles [61] and hcp structures for larger ones [62]. The truncated octahedron is more stable than the hcp up to 1900 atoms. The decahedron and cuboctahedron are considerably less stable, with a difference of 0.5 to 1 eV.atom$^{-1}$ compared to the three shapes mentioned before. Their curves of energies *vs.* size are nearly parallel, intersecting smoothly at 1300 atoms, where the cuboctahedron becomes more stable than the decahedron. We used the parameter $\Delta$, as introduced in Ref. [25], to depict the relative stabilities

in Fig. 6. This choice offers a clearer distinction between the various transitions compared to merely plotting linear regressions. The parameter $\Delta$ is defined as

$$\Delta(N) = \frac{E(N) - N\epsilon_{coh}}{N^{2/3}}, \tag{9}$$

where, $E(N)$ is the total energy of a nanoparticle containing $N$ atoms, and $\epsilon_{coh}$ the cohesive energy of bulk hcp cobalt, which is taken to be -7.04 eV.atom$^{-1}$.

Farkaš and de Leeuw [26] used DFT-PBE to minimize nanoparticles of different shapes up to 1000 atoms. They determined the relative stabilities of larger systems using a linear extrapolation. Their predictions are comparable to the results of the present explicit calculations, but there are noticeable differences: Farkaš and de Leeuw [26] predict the icosahedron to be the most stable shape up to 5500 atoms, followed by the hcp structure for larger nanoparticles. The present work predicts the transition at 3880 atoms. In Ref. [26] the transition between the truncated octahedron and hcp occurs near 500 atoms while the present results give 1879 atoms. In Ref. [26] the curves of the decahedron and cuboctahedron are separated by minimal differences in energy, but do not intersect while the explicit q-SNAP computations predict a transition at 1315 atoms, as can be seen from Fig. 6.

For comparison, the EAM potential [24] predicts the icosahedron to be the most stable shape up to 2666 atoms, with the transition between the truncated octahedron and hcp occurring near 387 atoms, which is consistent with the present results. However, the stability of the cuboctahedron is closer to that of the icosahedron, truncated octahedron, and hcp than to that of the decahedron. For small nanoparticles below 400 atoms, the EAM predicts the cuboctahedron to be even more stable than hcp, in disagreement with DFT-PBE calculations and the present q-SNAP results.

### B. Vacancy formation energy on vertices

Vacancy formation energies provide a sensitive test for the quality of interatomic potentials. To this end, a comparison was made between results from q-SNAP and the EAM potential as a function of the nanoparticle's size, focusing on the vertices of nanoparticles.

The vacancy formation energy is defined as

$$\Delta E_{\text{form,vac}} = E_{\text{tot,vac}} + (N^{-1} - 1)E_{\text{tot,clean}} \tag{10}$$

where $E_{\text{tot,clean}}$ is the total energy of the pristine nanoparticle without a vacancy, $E_{\text{tot,vac}}$ is the total energy of the nanoparticle with a vacancy, and $N$ is the number of atoms in the pristine nanoparticle [63].

According to both potentials, the vacancy formation energy decreases with an increasing number of atoms. The EAM potential predicts that forming a vacancy on a nanoparticle's vertex is always favorable, except for very small truncated octahedra and hcp nanoparticles,

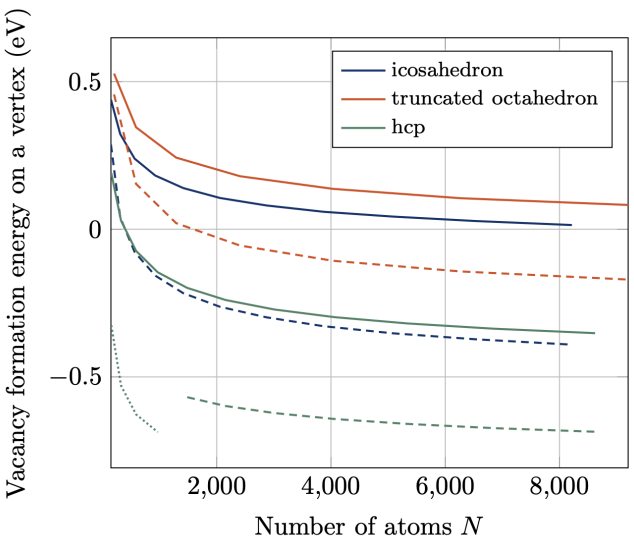


FIG. 7. (Color online) Vacancy formation energy on a vertex of icosahedra, truncated octahedra and hexagonal close packed nanoparticles according to their size. Results obtained with q-SNAP and EAM are drawn in solid and dashed lines, respectively. The green dotted line corresponds to the sizes where the EAM potential predicts the edge to be shifted in order to fill the vacancy, as illustrated in Fig. 8.

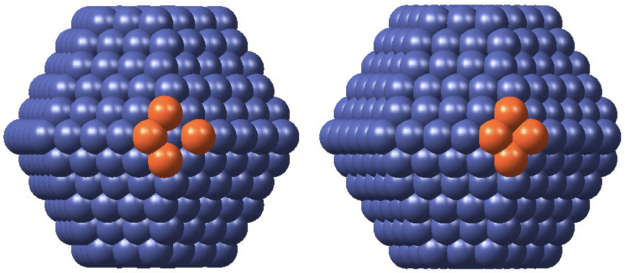

FIG. 8. (Color online) Hexagonal close-packed nanoparticle (587 atoms) minimized by the q-SNAP (left) and the EAM potential (right). Both q-SNAP and DFT-PBE predict minor deviations relative to the initial state (with one vertex removed from the minimized nanoparticle), wherein atoms surrounding the vacancy tend to move away from it. Conversely, the EAM potential predicts an edge shift to fill the vacancy.

whereas the q-SNAP predicts this behavior only for hcp nanoparticles containing more than 323 atoms, as shown in Fig. 7. For all sizes and shapes, the present q-SNAP predicts that the atoms surrounding the vacancy leave more space for it, while the EAM potential predicts the surrounding atoms to fill the vacancy. For hcp nanoparticles up to 967 atoms, the EAM potential even predicts that the entire edge is shifted to fill the vacancy, as illustrated on the right hand side of Fig. 8. For larger sizes, the edge does not shift, as predicted on the whole range according to the q-SNAP and for the hcp nanoparticle

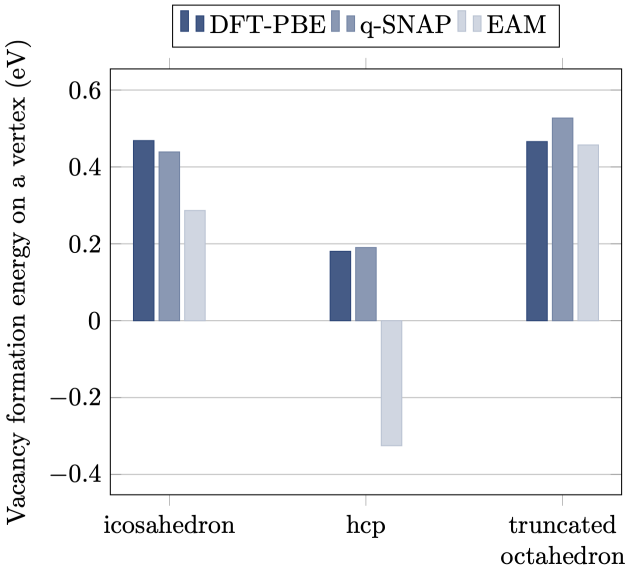


FIG. 9. (Color online) Vacancy formation energy on vertices of icosahedra, hexagonal close-packed and truncated octahedra of 147, 153 and 201 atoms respectively, calculated using DFT-PBE (dark blue), the q-SNAP (blue) and the EAM potential [24] (light blue).

of 153 atoms according to DFT-PBE. The two types of minimizations are represented by two distinct curves in Fig. 7. In addition, Fig. 9 illustrates the excellent agreement between the q-SNAP and DFT-PBE predictions for small nanoparticles.

### C. Melting

In atomistic simulations, it is possible to calculate the melting temperature of a material using the biphased cell method, as described above. It has also been demonstrated, both experimentally [64] and computationally [65], that it is possible to estimate the material's melting temperature by melting nanoparticles of varying sizes. As the size increases, the nanoparticle's melting temperature tends to that of the bulk. This phenomenon is described by the Gibbs-Thomson relation [64]:

$$T_{m,NP} = T_{m,b}\left(1 - \frac{C}{D}\right), \tag{11}$$

where $T_{m,NP}$ is the melting temperature of the nanoparticle with diameter $D$, $T_{m,b}$ is that of the bulk, and $C$ is a constant depending on the considered material. Thus, assuming the nanoparticle to be spherical, we deduce that the nanoparticle's melting temperature is inversely proportional to $N^{-\frac{1}{3}}$, where $N$ is the number of atoms in the nanoparticle:

$$T_{m,\mathrm{NP}} = T_{m,\mathrm{bulk}} - aN^{-\frac{1}{3}}, \tag{12}$$

where $a = T_{m,\mathrm{bulk}} \times C\left(\frac{\pi}{6}\right)^{\frac{1}{3}}$.

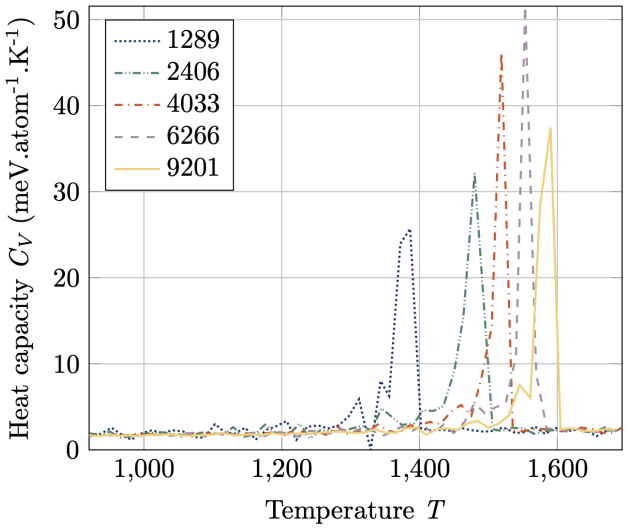


FIG. 10. (Color online) Heat capacities as a function of temperature for five truncated octahedra of increasing size. The maximum of the peak corresponds to the melting temperature.

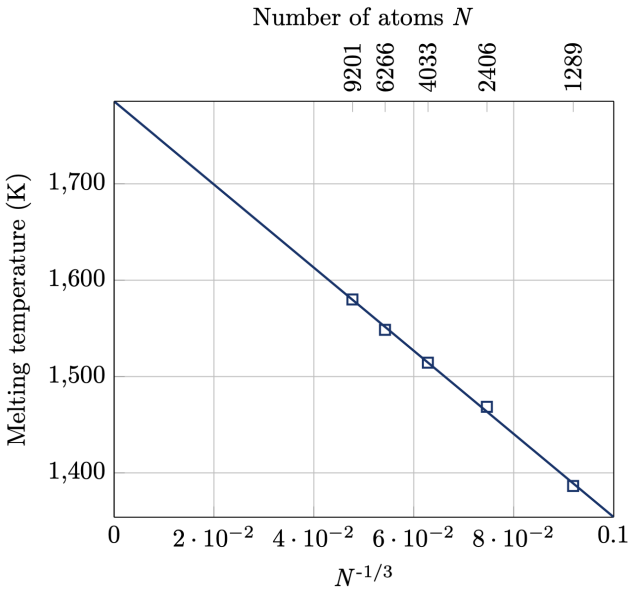


FIG. 11. (Color online) Linear fit (solid line) of truncated octahedral cobalt nanoparticles melting temperatures (squares) as a function of $N^{-1/3}$, where $N$ is the number of atoms. It leads to a bulk melting point of 1785 K, with a R-squared coefficient of 0.999.

This relationship is valid for large nanoparticles. In fact, experiments have shown that this relation does not hold for small nanoparticles [25, 66]. With a higher number of surface atoms compared to the bulk configuration, their behavior significantly deviates from that of the infinite system, making it unlikely that a straightforward extrapolation of macroscopic values will accurately predict

their properties. Thus, this study exclusively considers nanoparticles with sizes greater than 1000 atoms.

Above 693 K, bulk cobalt adopts a face-centered cubic structure. Therefore, to avoid shape effects and to be consistent with the determination of the melting temperature using the biphased cell method, the nanoparticles used in this study are perfect truncated octahedra containing 1289, 2406, 4033, 6266, and 9201 atoms, which correspond to the magic numbers of that shape. These nanoparticles are equilibrated at 900 K, then heated up to 2000 K with an overall heating rate of 0.08 $K.ps^{-1}$, in intervals of 5 K at constant temperature lasting 62.5 ps each. For these calculations, the system evolves through Langevin dynamics. The melting temperature corresponds to the maximum of the first derivative of the energy with respect to temperature, which was well defined in all cases, as shown in Fig. 10.

Extrapolation to infinitely large particles using the linear fit of the nanoparticles' melting points, as illustrated in Fig. 11, yields a bulk melting point of 1785 K, a mere 15 K higher than the experimental melting point. This outcome underscores the present q-SNAP's exceptional ability to accurately capture the dynamics of cobalt nanoparticles. It implicitly also demonstrates that the DFT-PBE level of theory captures the free energy difference between solid and liquid Co remarkably well.

## IV. CONCLUSION

In this article we presented the development, validation, and capabilities of a q-SNAP to predict static and dynamic properties of bulk Co, its surfaces, and nanoparticles.

The training set consisted of a total of 1049 cobalt structures, encompassing diverse crystallographic lattices with varying degrees of deformation, submitted to molecular dynamics at various temperatures and pressures, as well as surfaces and nanoparticles deliberately displaced from their equilibrium states to capture a wide range of atomic environments.

While the computational cost associated with obtaining the training set may seem significant, it is quickly offset by the new capabilities gained once the q-SNAP is operational. This potential enables simulations of several dozens of nanoseconds, involving thousands of atoms, while closely maintaining the precision of DFT-PBE. The present q-SNAP reproduces remarkably well atomic vibrations (phonon dispersions) compared with results from DFT-PBE calculations, thus enabling accurate predictions of quantities such as thermal expansion, the hcp-fcc phase transition temperature, and the melting point. The values obtained for these properties with q-SNAP are in remarkable agreement with experimental data, thus implicitly validating the accuracy of the underlying DFT-PBE level of theory.

Given its precise reproduction of DFT surface energies, one expects its aptitude in correctly modeling nanoparticles, which indeed is demonstrated in the present work. It accurately reproduces static properties such as the relative stability of nanoparticles of different shapes as a function of their size. Calculations of the vacancy formation energy on vertices of nanoparticles and related subtle structural changes demonstrate the high sensitivity of the present q-SNAP. Its robustness is further illustrated by accurately extrapolating melting temperatures of nanoparticles to the bulk value as a function of the number of atoms.

This diverse range of capabilities positions the q-SNAP as a promising tool for catalysis applications, particularly due to its versatility in accommodating additional elements of various types—an advantage not shared by EAM potentials, which are restricted mostly to metals.

The DFT calculations of the training set use a spin-polarized Hamiltonian. In all of the present configurations, the spins are ordered ferromagnetically. This facilitates the correlation between the structural environment and SNAP descriptors, which lack explicit information on magnetic moments. For other transition metals with lower Curie temperatures, such as iron, accounting for magnetic ordering becomes important. The development of machine-learned potentials including magnetism has been demonstrated for pure Fe [67]. The extension to systems with multiple magnetic elements is a field of ongoing and leading research.

It is important to note that the present q-SNAP was specifically constructed to model hcp and fcc cobalt, along with their surfaces and nanoparticles in various structures. Caution must be exercised when employing machine-learned potentials to simulate systems significantly different from the training set.

In conclusion, the present work demonstrates that current machine-learned potentials are able to reach near DFT accuracy at the speed of conventional interatomic potentials, accurately capturing subtle dynamic effect such as the structure, energetics, and dynamics of surface atoms on nanoparticles.

The newly developed potential used in the present work can be downloaded from Ref. [68].

## ACKNOWLEDGMENTS

We would like to thank Dr. Farkaš from Cardiff University and Dr. de Leeuw from Utrecht University for providing the structural data of small cobalt nanoparticles [26] used in our training set. Their contribution was greatly appreciated.

Finally, we would like to thank all colleagues at Materials Design, especially Xavier Rozanska, for their help and support of this work.

[1] H. Matter, J. Winter, and W. Triftshäuser, Phase transformations and vacancy formation energies of transition metals by positron annihilation, Appl. Phys. **20**, 135 (1979).

[2] M. S. Van Dusen and A. I. Dahl, Freezing points of cobalt and nickel and a new determination of Planck's constant C2, Science **106**, 428 (1947).

[3] D. Coutsouradis, A. Davin, and M. Lamberigts, Cobalt-based superalloys for applications in gas turbines, Materials Science and Engineering **88**, 11 (1987).

[4] N. Nitta, F. Wu, J. T. Lee, and G. Yushin, Li-ion battery materials: present and future, Materials Today **18**, 252 (2015).

[5] J. Ariake, T. Chiba, S. Watanabe, N. Honda, and K. Ouchi, Magnetic and structural properties of Co–Pt perpendicular recording media with large magnetic anisotropy, Journal of Magnetism and Magnetic Materials **287**, 229 (2005).

[6] K. J. Strnat and R. M. W. Strnat, Rare earth-cobalt permanent magnets, Journal of Magnetism and Magnetic Materials **100**, 38 (1991).

[7] B. Patel, G. Favaro, F. Inam, M. J. Reece, A. Angadji, W. Bonfield, J. Huang, and M. Edirisinghe, Cobalt-based orthopaedic alloys: Relationship between forming route, microstructure and tribological performance, Materials Science and Engineering: C **32**, 1222 (2012).

[8] M. Kassapidou, V. F. Stenport, C. B. Johansson, M. Syverud, P. Hammarström Johansson, J. Börjesson, and L. Hjalmarsson, Cobalt chromium alloys in fixed prosthodontics: Investigations of mechanical properties and microstructure, The Journal of Prosthetic Dentistry **130**, 255e1 (2023).

[9] L. J. Schreiner, C. P. Joshi, J. Darko, A. Kerr, G. Salomons, and S. Dhanesar, The role of Cobalt-60 in modern radiation therapy: Dose delivery and image guidance, Journal of Medical Physics / Association of Medical Physicists of India **34**, 133 (2009).

[10] K. Sato, S.-I. Miyahara, K. Tsujimaru, Y. Wada, T. Toriyama, T. Yamamoto, S. Matsumura, K. Inazu, H. Mohri, T. Iwasa, T. Taketsugu, and K. Nagaoka, Barium oxide encapsulating cobalt nanoparticles supported on magnesium oxide: Active non-noble metal catalysts for ammonia synthesis under mild reaction conditions, ACS Catal. **11**, 13050 (2021).

[11] D. Astruc, Introduction: Nanoparticles in catalysis, Chem. Rev. **120**, 461 (2020).

[12] W. Kohn and L. J. Sham, Self-consistent equations including exchange and correlation effects, Phys. Rev. **140**, A1133 (1965).

[13] M. S. Daw and M. I. Baskes, Embedded-atom method: Derivation and application to impurities, surfaces, and other defects in metals, Phys. Rev. B **29**, 6443 (1984).

[14] V. L. Deringer, M. A. Caro, and G. Csányi, Machine learning interatomic potentials as emerging tools for materials science, Advanced Materials **31**, 1902765 (2019).

[15] J. Behler and M. Parrinello, Generalized neural-network representation of high-dimensional potential-energy surfaces, Phys. Rev. Lett. **98**, 146401 (2007).

[16] V. Eyert, J. Wormald, W. A. Curtin, and E. Wimmer, Machine-learned interatomic potentials: Recent developments and prospective applications, Journal of Materials Research **38**, 5079 (2023).

[17] A. P. Bartók, M. C. Payne, R. Kondor, and G. Csányi, Gaussian approximation potentials: The accuracy of quantum mechanics, without the electrons, Phys. Rev. Lett. **104**, 136403 (2010).

[18] A. P. Bartók, R. Kondor, and G. Csányi, On representing chemical environments, Phys. Rev. B **87**, 184115 (2013).

[19] R. Drautz, Atomic cluster expansion for accurate and transferable interatomic potentials, Phys. Rev. B **99**, 014104 (2019).

[20] A. P. Thompson, L. P. Swiler, C. R. Trott, S. M. Foiles, and G. J. Tucker, Spectral neighbor analysis method for automated generation of quantum-accurate interatomic potentials, Journal of Computational Physics **285**, 316 (2015).

[21] A. M. Goryaeva, J. Dérès, C. Lapointe, P. Grigorev, T. D. Swinburne, J. R. Kermode, L. Ventelon, J. Baima, and M.-C. Marinica, Efficient and transferable machine learning potentials for the simulation of crystal defects in bcc Fe and W, Phys. Rev. Mater. **5**, 103803 (2021).

[22] H. Gassner, M. Probst, A. Lauenstein, and K. Hermansson, Representation of intermolecular potential functions by neural networks, J. Phys. Chem. A **102**, 4596 (1998).

[23] M. A. Wood and A. P. Thompson, Extending the accuracy of the SNAP interatomic potential form, J. Chem. Phys. **148**, 241721 (2018).

[24] G. P. P. Pun and Y. Mishin, Embedded-atom potential for hcp and fcc cobalt, Phys. Rev. B **86**, 134116 (2012).

[25] F. Baletto and R. Ferrando, Structural properties of nanoclusters: Energetic, thermodynamic, and kinetic effects, Rev. Mod. Phys. **77**, 371 (2005).

[26] B. Farkaš and N. H. de Leeuw, Towards a morphology of cobalt nanoparticles: size and strain effects, Nanotechnology **31**, 195711 (2020).

[27] G. Kresse and J. Furthmüller, Efficient iterative schemes for ab initio total-energy calculations using a plane-wave basis set, Phys. Rev. B **54**, 11169 (1996).

[28] G. Kresse and J. Furthmüller, Efficiency of ab initio total energy calculations for metals and semiconductors using a plane-wave basis set, Computational Materials Science **6**, 15 (1996).

[29] J. P. Perdew, K. Burke, and M. Ernzerhof, Generalized gradient approximation made simple, Phys. Rev. Lett. **77**, 3865 (1996).

[30] D. C. Langreth and M. J. Mehl, Beyond the local-density approximation in calculations of ground-state electronic properties, Phys. Rev. B **28**, 1809 (1983).

[31] MedeA 3.8; MedeA is a registered trademark of Materials Design, Inc., San Diego, USA. (2023).

[32] G. Kresse and D. Joubert, From ultrasoft pseudopotentials to the projector augmented-wave method, Phys. Rev. B **59**, 1758 (1999).

[33] M. Methfessel and A. T. Paxton, High-precision sampling for brillouin-zone integration in metals, Phys. Rev. B **40**, 3616 (1989).

[34] Y. Mishin, Machine-learning interatomic potentials for materials science, Acta Materialia **214**, 116980 (2021).

[35] W. B. Pearson, *A handbook of lattice spacings and structures of metals and alloys*, 1st ed., Vol. 2 (Pergamon Press, Oxford, 1967).

[36] D. Antonangeli, M. Krisch, G. Fiquet, D. L. Farber,

C. M. Aracne, J. Badro, F. Occelli, and H. Requardt, Elasticity of cobalt at high pressure studied by inelastic x-ray scattering, Phys. Rev. Lett. **93**, 215505 (2004).
[37] G. Simmons and H. Wang, *Single Crystal Elastic Constants and Calculated Aggregate Properties*, 2nd ed. (The MIT Press, 1971).
[38] H. J. McSkimin, Measurement of the elastic constants of single crystal cobalt, Journal of Applied Physics **26**, 406 (1955).
[39] F. De Boer, R. Boom, W. Mattens, A. Miedema, and A. Niessen, *Cohesion in Metals: Transition Metal Alloys* (North-Holland, 1988).
[40] D. E. Laughlin and K. Hono, *Physical Metallurgy*, 5th ed. (Elsevier, 2015).
[41] Y. S. Touloukian, R. K. Kirby, R. E. Taylor, and P. D. Desai, *Thermophysical properties of matter - the TPRC data series. Volume 12. Thermal expansion metallic elements and alloys.*, Tech. Rep. AD-A-129115/2/XAB (Purdue Univ., Lafayette, IN (United States). Thermophysical and Electronic Properties Information Center, 1975).
[42] K. Schäfer, Selected values of thermodynamic properties of metals and alloys, Angewandte Chemie **77**, 468 (1965).
[43] A. Fernández Guillermet, Critical evaluation of the thermodynamic properties of cobalt, Int J Thermophys **8**, 481 (1987).
[44] W. M. Haynes, *CRC Handbook of Chemistry and Physics* (Taylor & F, 2014).
[45] W. Gale and T. Totemeier, *Smithells Metals Reference Book*, 8th ed. (Elsevier, 2004).
[46] W. Welford, Elastic, piezoelectric, pyroelectric, piezooptic, electrooptic constants, and nonlinear dielectric susceptibilities of crystals, Optica Acta: International Journal of Optics **26**, 1133 (1979).
[47] J. Gump, H. Xia, M. Chirita, R. Sooryakumar, M. A. Tomaz, and G. R. Harp, Elastic constants of face-centered-cubic cobalt, Journal of Applied Physics **86**, 6005 (1999).
[48] B. Strauss, F. Frey, W. Petry, J. Trampenau, K. Nicolaus, S. M. Shapiro, and J. Bossy, Martensitic phase transformation and lattice dynamics of fcc cobalt, Phys. Rev. B **54**, 6035 (1996).
[49] H. Ullmaier, ed., *Atomic Defects in Metals*, Vol. 25 (Springer-Verlag, Berlin, Heidelberg, 1991).
[50] M. R. LaBrosse, L. Chen, and J. K. Johnson, First principles study of vacancy and tungsten diffusion in fcc cobalt, Modelling Simul. Mater. Sci. Eng. **18**, 015008 (2009).
[51] C. Kittel, *Introduction to solid state physics*, 8th ed. (Wiley, Hoboken, NJ, 2005).
[52] A. P. Thompson, H. M. Aktulga, R. Berger, D. S. Bolintineanu, W. M. Brown, P. S. Crozier, P. J. in 't Veld, A. Kohlmeyer, S. G. Moore, T. D. Nguyen, R. Shan, M. J. Stevens, J. Tranchida, C. Trott, and S. J. Plimpton, LAMMPS - A flexible simulation tool for particle-based materials modeling at the atomic, meso, and continuum scales, Computer Physics Communications **271**, 108171 (2022).
[53] P. Lazar and M. Otyepka, Accurate surface energies from first principles, Phys. Rev. B **91**, 115402 (2015).
[54] K. Parlinski, Z. Q. Li, and Y. Kawazoe, First-principles determination of the soft mode in cubic $ZrO_2$, Phys. Rev. Lett. **78**, 4063 (1997).
[55] N. Wakabayashi, R. H. Scherm, and H. G. Smith, Lattice dynamic of Ti, Co, Tc, and other hcp transition metals, Phys. Rev. B **25**, 5122 (1982).
[56] P. H. Berens, D. H. J. Mackay, G. M. White, and K. R. Wilson, Thermodynamics and quantum corrections from molecular dynamics for liquid water, The Journal of Chemical Physics **79**, 2375 (1983).
[57] S.-T. Lin, M. Blanco, and W. A. Goddard, III, The two-phase model for calculating thermodynamic properties of liquids from molecular dynamics: Validation for the phase diagram of Lennard-Jones fluids, The Journal of Chemical Physics **119**, 11792 (2003).
[58] J. R. Espinosa, E. Sanz, C. Valeriani, and C. Vega, On fluid-solid direct coexistence simulations: the pseudo-hard sphere model, J Chem Phys **139**, 144502 (2013).
[59] M. Boudart, Catalysis by supported metals, in *Advances in Catalysis*, Vol. 20, edited by D. D. Eley, H. Pines, and P. B. Weisz (Academic Press, 1969) pp. 153–166.
[60] L. Bonati, D. Polino, C. Pizzolitto, P. Biasi, R. Eckert, S. Reitmeier, R. Schlögl, and M. Parrinello, The role of dynamics in heterogeneous catalysis: Surface diffusivity and $N_2$ decomposition on Fe(111), Proceedings of the National Academy of Sciences **120**, e2313023120 (2023).
[61] T. D. Klots, B. J. Winter, E. K. Parks, and S. J. Riley, Icosahedral structure in hydrogenated cobalt and nickel clusters, The Journal of Chemical Physics **95**, 8919 (1991).
[62] A. F. Khusnuriyalova, M. Caporali, E. Hey-Hawkins, O. G. Sinyashin, and D. G. Yakhvarov, Preparation of cobalt nanoparticles, European Journal of Inorganic Chemistry **2021**, 3023 (2021).
[63] C. Mottet, G. Tréglia, and B. Legrand, New magic numbers in metallic clusters: an unexpected metal dependence, Surface Science **383**, L719 (1997).
[64] S. L. Lai, J. R. A. Carlsson, and L. H. Allen, Melting point depression of Al clusters generated during the early stages of film growth: Nanocalorimetry measurements, Applied Physics Letters **72**, 1098 (1998).
[65] Ph. Buffat and J.-P. Borel, Size effect on the melting temperature of gold particles, Phys. Rev. A **13**, 2287 (1976).
[66] P. Labastie and F. Calvo, Thermodynamics and solid—liquid transitions, in *Nanomaterials and Nanochemistry* (Springer, Berlin, Heidelberg, 2008) pp. 55–87.
[67] M. Rinaldi, M. Mrovec, A. Bochkarev, Y. Lysogorskiy, and R. Drautz, Non-collinear magnetic atomic cluster expansion for iron, npj Comput Mater **10**, 1 (2024).
[68] The URL will be active once the paper is published.